14th International Symposium on Turbulence and Shear Flow Phenomena (TSFP14)
Heidelberg, Germany, July 28–31, 2026

HEAT TRANSFER AND DYNAMICS OF SECONDARY MOTIONS OVER STREAMWISE-ALIGNED RIDGES

Kay Schäfer
Meteorological Institute
University of Hamburg
Hamburg, Germany
kay.schaefer@uni-hamburg.de

Juan Pedro Mellado
Meteorological Institute
University of Hamburg
Hamburg, Germany
juan.pedro.mellado@uni-hamburg.de

INTRODUCTION

Turbulent large-scale structures occur in a wide range of technical and environmental flows. A prominent example is the formation of convective rolls in the atmospheric boundary layer. These structures are made visible by the formation of cloud streets in the updraft region of the rolls, where water vapour condensation and cloud formation concentrates (LeMone, 1973). These convective rolls are large-scale counter-rotating vortices that affect the entire boundary layer depth, highlighting the importance of turbulent large-scale structures on the distribution of scalars, such as water vapour, aerosols and pollutants. The presence of large-scale structures also violates common assumptions made for surface-flux parametrizations in weather and climate models, which is based on the Monin-Obukhov similarity theory (Wyngaard, 2010; Bou-Zeid *et al.*, 2020).

A particularly important and challenging aspect of turbulent large-scale structures is how they are affected or triggered by surface heterogeneity and roughness. In this regard, another interesting type of turbulent large-scale structure is turbulent secondary motions which are initiated by spanwise surface heterogeneities and which have received special attention in recent years and are the subject of fundamental research. Secondary motions appear in the mean velocity field as counter-rotating vortices filling the entire flow depth and which are located at the transition of the surface heterogeneity. They can form for example over streamwise-aligned ridges or spanwise alternating rough and smooth-wall strips, which are referred to as ridge- and strip-type surfaces, respectively (Wang & Cheng, 2006; Stroh *et al.*, 2020*b*).

Recent studies have investigated how secondary motions interact with or are related to other turbulent large-scale structures. Different coexistence between secondary motions and naturally occurring very-large-scale motions (VLSM) has been observed for ridge- and strip-type surfaces. Strip-type surfaces allow coexistence between both types of structures, and it is speculated that secondary motions might be spanwise-locked VLSMs (Wangsawijaya *et al.*, 2020). On the other hand, ridge-type induced secondary motions suppress the formation of VLSMs, thus leaving their relationship ambiguous (Zampiron *et al.*, 2020). For mixed convection flows it was found that turbulent secondary motions cannot coexist with convective rolls, and they are suppressed by convective rolls already at mild stratification levels (Schäfer *et al.*, 2022). At the same time, the transition regime of convective rolls is drastically modified by the presence of streamwise-aligned ridges.

A second aspect of turbulent large-scale structures and secondary motions that is considered here is the heat transfer. Even though a better understanding of the heat and mass transfer over heterogeneous surfaces is critical for climate modelling (Bou-Zeid *et al.*, 2020), the effects of spanwise heterogeneous surfaces and secondary motions on this has gained little attention so far. For a specific ridge-type configuration the secondary motions were found to increase the momentum and heat transfer in a turbulent channel flow by up to 30% (Stroh *et al.*, 2020*a*). However, a systematic study on surface parameter variations and its impact on the heat transfer of secondary motions is missing to date.

This study addresses these two aspects of the interaction between turbulent large-scale structures and secondary motions. On the one hand, it will contribute to a better understanding of the heat transfer of secondary motions by performing direct numerical simulations (DNS) of ridge-type surfaces with systematic surface parameter variations. On the other hand, the coexistence between secondary motions and naturally occurring VLSMs is further examined by using sufficiently high Reynolds number. In conjunction with the surface parameter variations this will shed further light on how heterogeneous surfaces manipulate the interaction between secondary motions and VLSMs.

METHODOLOGY

We perform DNS of a fully developed turbulent open-channel flow with streamwise-aligned ridges at the bottom wall, which is depicted in figure 1. The effective friction Reynolds number $Re_{\tau,\mathrm{eff.}}$, which is based on the effective domain height $\delta_{\mathrm{eff.}}$ taking into account the reduced cross-sectional area in presence of ridges, is varied between $Re_{\tau,\mathrm{eff.}} = 180 - 1000$. In addition, a passive scalar transport

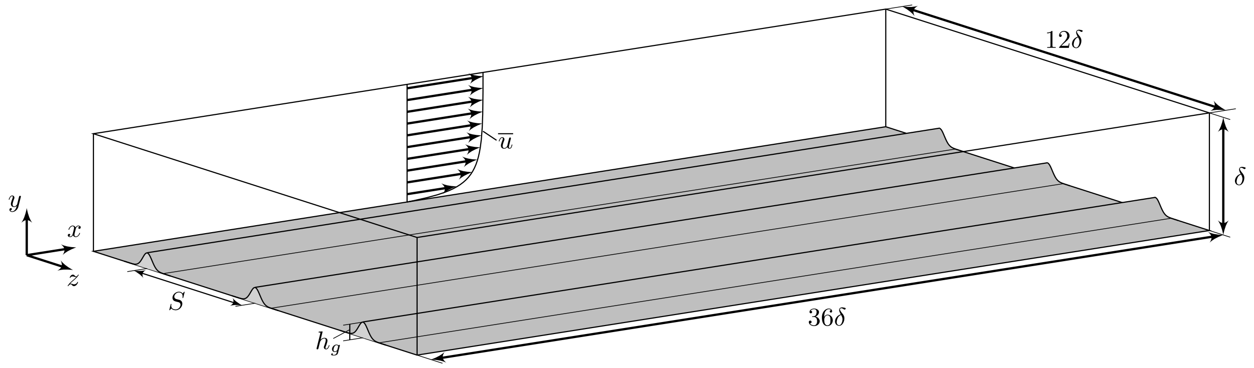

Figure 1. Schematic of open-channel flow domain with streamwise aligned Gaussian ridges.

equation is solved, which in the following will be termed temperature (though the results are applicable to any kind of passive scalar) with a chosen Prandtl number $Pr = 1$. In the horizontal directions periodic boundary conditions are used. The momentum equation employs in wall-normal direction no-slip and symmetry boundary conditions at the bottom wall and top domain, respectively. For the temperature equation, a constant bottom wall value and a zero-flux conditions at the top of the domain are imposed and a source term is added to maintain the volume-averaged temperature at a fixed value. A large horizontal domain size of $L_x \times L_z = 36\delta \times 12\delta$ is used, to allow for the formation of VLSMs (Bauer *et al.*, 2024). The grid resolution in streamwise, wall-normal and spanwise direction for the $Re_{\tau,\mathrm{eff.}} = 540$ and $Re_{\tau,\mathrm{eff.}} = 1000$ cases are $N_x \times N_y \times N_z = 3072 \times 257 \times 1152$ and $N_x \times N_y \times N_z = 5120 \times 385 \times 2304$, respectively.

The streamwise-aligned ridges have a Gaussian contour (Schäfer *et al.*, 2022), with a fixed width and the ridge height is varied between $h_g = 0.025\delta - 0.1\delta$. In addition, the ridge spacing S is varied to allow for different regimes between the interaction of secondary motions and VLSMs as observed by Zampiron *et al.* (2020).

The Navier-Stokes equations are solved by means of the open-source code Xcompact3d (Bartholomew *et al.*, 2020). The spatial discretization is based on sixth-order compact-finite differences and time integration is performed with a third-order Runge-Kutta method. The ridges are numerically represented by an immersed boundary method (IBM) which is based on a high order polynomial reconstruction method in order to allow for a smooth solution between the solid and fluid interface for the compact finite derivatives (Gautier *et al.*, 2014).

The velocity and temperature fields are decomposed using a triple decomposition as:

$$u_i(x,y,z,t) = \langle \overline{u}_i \rangle (y) + \tilde{u}_i(y,z) + u_i''(x,y,z,t) \quad (1)$$

$$= \langle \overline{u}_i \rangle (y) + u_i'(x,y,z,t) \quad (2)$$

where $\langle \overline{u}_i \rangle$ denotes the temporally, streamwise, and spanwise averaged velocity field, $\tilde{u}_i$ represents the coherent part, defined as the spatial variation in z around $\langle \overline{u}_i \rangle$, and u_i'' corresponds to the random fluctuation. The turbulent fluctuation u_i' is obtained by combining the coherent and random components. Throughout this work, streamwise and temporal averaging are denoted by $\bar{\cdot}$, while spanwise averaging is denoted by $\langle \cdot \rangle$.

RESULTS

The formation of turbulent secondary motions over spanwise heterogeneous surfaces is depicted by the time- and streamwise-averaged velocity $\overline{u}$ and scalar field $\overline{T}$ for $Re_{\tau,\mathrm{eff.}} = 540$ in figure 2. The secondary motions appear as counter-rotating vortices centered with their upward motion at the ridges. For the ridge height cases $h_g = 0.05\delta$ and $h_g = 0.1\delta$ the secondary motions appear as large-scale vortices reaching up to the half-channel height and introducing a low-momentum region (LMR) characterized by the strong upward bulging of $\overline{u}$. Similarly, the secondary motions transport high temperature from near the surface upwards, leading to a similar bulging for $\overline{T}$. The smallest ridge height case $h_g = 0.025\delta$ ($h_g^+ = 13.5$) shows only a gentle upward bulging of $\overline{u}$ and $\overline{T}$ at the ridge location, indicating that the formation of secondary motions is inhibited when large parts of the ridge are predominantly immersed in the viscous sublayer.

The shown ridge spacing of $S = 4\delta$ in figure 2 depicts an additional and weak upward bulging of $\overline{u}$ and $\overline{T}$ at the center between neighbouring ridges with a small pair of counter-rotating vortices, which is referred to as tertiary motions (Vanderwel & Ganapathisubramani, 2015). Even though these tertiary motions are present, we observe the formation of VLSMs in this region. However, the strength of VLSMs, as further quantified by the pre-multiplied streamwise energy spectra in figure 4 (a), is weaker than observed for smooth wall conditions. For denser ridge spacings $S \leq 2\delta$ and $h_g = 0.1\delta$, we confirm the experimental observations by Zampiron *et al.* (2020), that ridges with $h_g \approx 0.1\delta$ suppress the formation of VLSMs in the entire channel. However, reducing the ridge height allows for a strengthening of the VLSMs in the valley region for $h_g = 0.05\delta$ and eventually for $h_g = 0.025\delta$ also for the reappearance above the ridges (Schäfer, 2023).

The spatial organization of the instantaneous flow structures is further illustrated in figure 3, which presents the streamwise velocity fluctuation u' and temperature fluctuation T' in the horizontal midplane at $y = 0.5\delta$. In the smooth-wall case, well-developed VLSMs are observed, manifested as elongated and meandering low- and high-momentum regions (LMRs/HMRs) extending across the full streamwise extent of the domain. For the ridge case $S = 4\delta$ and $h_g = 0.1\delta$, pronounced LMRs are located at the ridge positions, while long high-momentum streaks reminiscent of smooth-wall VLSMs persist in the center of the valley region. The case $h_g = 0.05\delta$ exhibits noticeably weaker LMRs at the ridge location, which nonetheless retain a considerable streamwise coherence. For $h_g = 0.025\delta$, only subtle LMRs are discernible at the ridge positions and the overall flow field closely resembles the smooth-wall case. The instantaneous temperature fluctuation field

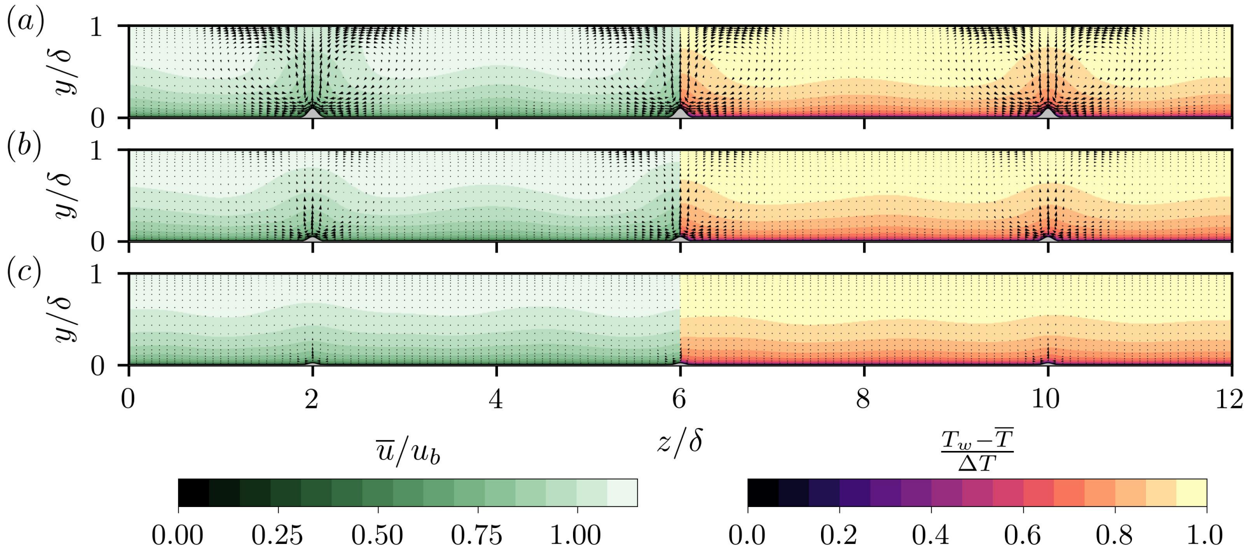

Figure 2. Formation of mean secondary motions in the channel cross-section and the effect of ridge height h_g variations. The friction Reynolds number is $Re_\tau = 540$ and the spanwise ridge spacing is $S = 4\delta$. The ridge height is $h_g = 0.1\delta$ in (a), $h_g = 0.05\delta$ in (b) and $h_g = 0.025\delta$ in (c). The black arrows represent the cross-sectional velocity components.

shares qualitative similarities with the streamwise velocity, with elevated temperature coinciding with LMRs and reduced temperature with HMRs. However, the temperature structures exhibit finer spatial scales and a shorter streamwise coherence compared to the velocity field.

The spanwise distribution of VLSM energy is examined in figure 4 (a), which shows the one-dimensional pre-multiplied streamwise energy spectra $\kappa_x \Phi_{u''u''}$ at $y = 0.5\delta$ for different ridge heights h_g at fixed $S = 4\delta$.

The one-dimensional power spectral density is defined by

$$\langle \overline{u''u''} \rangle (y,z) = \int_0^\infty \Phi_{u''u''}(\kappa_x, y, z)\, \mathrm{d}\kappa_x. \tag{3}$$

In the smooth-wall reference case ($S = \infty$), significant VLSM energy contributions ($\lambda_x \geq 18\delta$) are present across the entire channel width, with individual spectral peaks arising from the finite temporal integration of the simulation. For $S = 4\delta$ and $h_g = 0.1\delta$, VLSMs are suppressed above the ridges and can only be observed in an attenuated form within the valley regions compared to the smooth-wall case. For $h_g = 0.05\delta$, energized wavelengths in the range $\lambda_x \approx 2\delta$–$5\delta$ remain detectable at the ridge positions, along with regions of reduced spectral energy on either side of the ridges, a feature that becomes indistinct for $h_g = 0.025\delta$. In the latter case, VLSMs are capable of forming above the ridge locations, indicating that sufficiently small ridges no longer impose a lateral barrier to VLSM development, consistent with smooth-wall behaviour. Figure 4 (b) presents the corresponding pre-multiplied temperature spectra $\kappa_x \Phi_{T''T''}$ at $y = 0.5\delta$. The dominant temperature fluctuation energy is concentrated at wavelengths around $\lambda_x \approx \delta$, which are considerably shorter than the energetically dominant scales in the streamwise velocity spectra, consistent with the finer spatial scales of the temperature structures visible in figure 3. The wavelength range of peak temperature spectral energy correlates well with that of the vertical velocity spectra, suggesting that temperature fluctuations are primarily generated by vertical mixing induced by the secondary motions. Analogous to the velocity spectra, the spectral energy above the ridges decreases with decreasing ridge height h_g.

The effect of Re_τ and S on the skin friction coefficient C_f and Nusselt number Nu is shown in figure 5. The steady decrease of S leads to a monotonic increase of C_f and Nu compared to the smooth-wall case. For example for $Re_{\tau,\text{eff.}} = 1000$ and $S = 0.5\delta$ this results in an increase of C_f by 16.8% and Nu by 7.5%. The Gnielinski correlation for uniform wall temperature and uniform heat flux from pipe flows (Gnielinski, 1976) is used for comparison with the present Nu data, and provides a reasonable fit for the smooth wall open-channel flow cases. This correlation reads

$$Nu = \frac{(C_f/2)(4Re_b - 1000)\, Pr}{1 + 12.7\,(C_f/2)^{1/2}(Pr^{2/3} - 1)}, \tag{4}$$

where Re_b is the bulk Reynolds number and Pr the Prandtl number. For the smooth-wall case, C_f is provided by the correlation of Pope (2000),

$$C_f = 0.0336 \cdot Re_\tau^{-3/11}, \tag{5}$$

which serves as the baseline for the present ridge cases. For the ridge cases with $h_g = 0.1\delta$, we propose a modified correlation for C_f that accounts for the ridge spacing S and recovers equation 5 asymptotically as $S \to \infty$, reading

$$C_f = 0.0336 \cdot \left(1 + \frac{0.1076}{S}\right) \cdot Re_\tau^{-3/11}. \tag{6}$$

This correlation is shown for the different ridge spacings S in figure 5 (a), with a maximum deviation from the simulation data of 4.12%. The Gnielinski correlation is then evaluated using equation 6 for the ridge cases, yielding a maximum deviation in Nu below 3.98%, as shown in figure 5 (b). The proposed correlations provide a good overall fit to the simulation data, with marginally improved agreement at lower

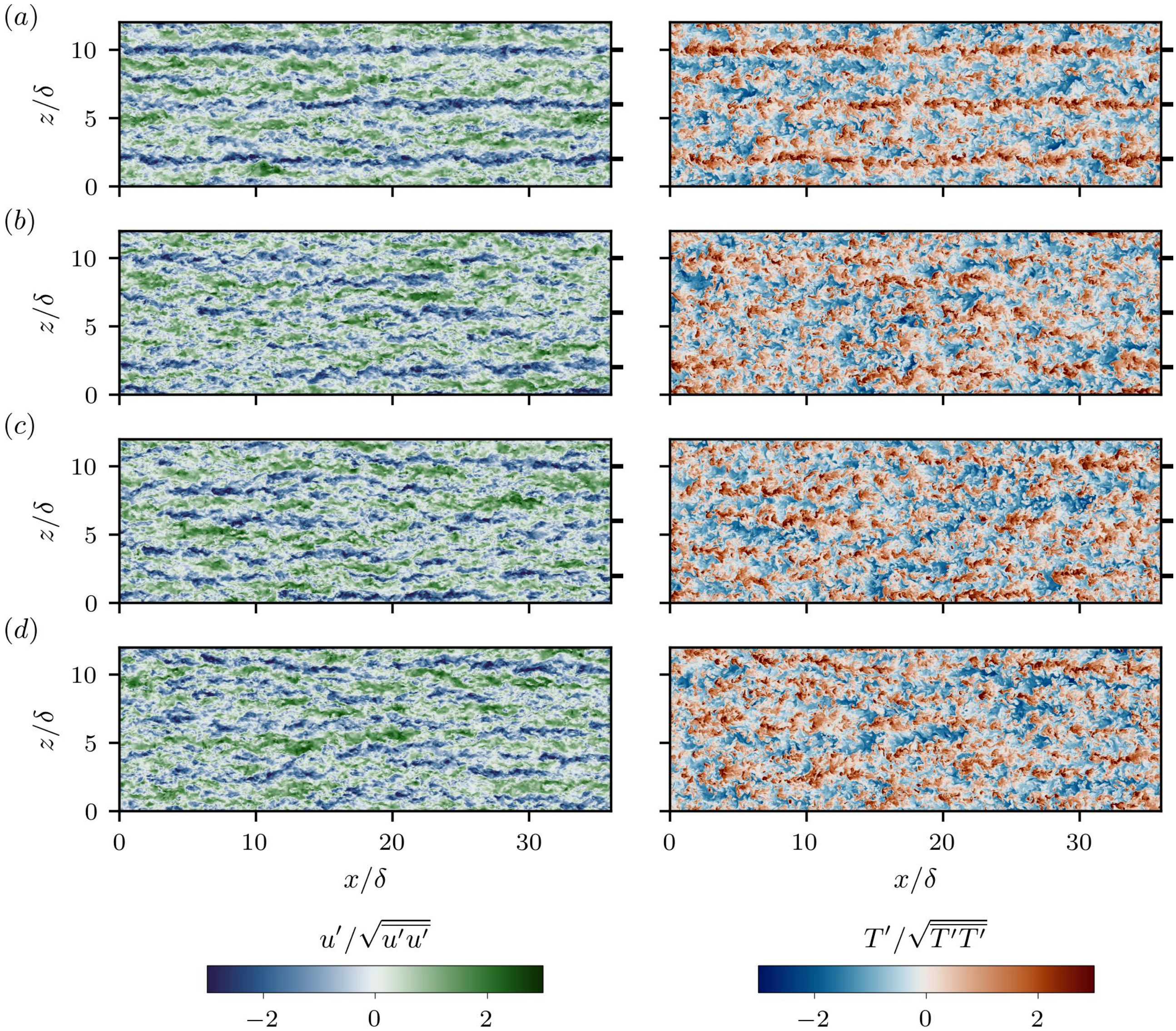

Figure 3. Instantaneous streamwise velocity fluctuations in left panel and temperature fluctuations in right panel side in a horizontal plane at $y = 0.5\delta$ for $Re_\tau = 540$ and $S = 4\delta$ and varying ridge heights h_g. Gaussian ridge cases are $h_g = 0.1\delta$ (a), $h_g = 0.05\delta$ (b), $h_g = 0.025\delta$ (c) and the smooth wall case is shown in (d). The black horizontal lines at the outer right figure frame indicate the spanwise position of the ridges.

Reynolds numbers, suggesting that additional high-Reynolds-number data could further refine the proposed expressions. Future work will be devoted to extending these correlations to incorporate ridge height variations and to provide a more general parametrisation of Nu for different ridge configurations.

CONCLUSION & OUTLOOK

The present study investigates turbulent secondary motions over streamwise-aligned ridges in a turbulent open-channel flow. Different ridge arrangements in form of varying ridge spacings S and ridge heights h_g are analyzed to study their impact on the transfer coefficients, as well as how these surface parameters are decisive for the interaction and coexistence between secondary motions and naturally occurring VLSMs. It is shown that the heat transfer of secondary motions is monotonically increased by decreasing S. For ridge cases with $h_g = 0.1\delta$, a modified C_f correlation incorporating the ridge spacing S is proposed, which is subsequently employed in the Gnielinski correlation to obtain Nu predictions; both show good agreement with the simulation data within deviations of approximately 4%. Further work will be devoted to extending these correlations to include ridge height variations, providing an improved surface parametrisation for heterogeneous surfaces. Regarding the interaction between secondary motions and VLSMs, we find that the ridge height h_g plays a critical role in the suppression of VLSMs. Analysis of instantaneous flow fields and pre-multiplied energy spectra demonstrates that sufficiently small ridges no longer act as a lateral barrier to VLSM development, and the flow recovers a spatial organisation resembling smooth-wall conditions. Thus, the different interactions observed for ridge- and strip-type surfaces might be related to the different vertical forcing induced by the ridges and the resulting strength of secondary motions.

REFERENCES

Bartholomew, P., Deskos, G., Frantz, R. A. S., Schuch, F. N., Lamballais, E. & Laizet, S. 2020 Xcompact3D: An open-

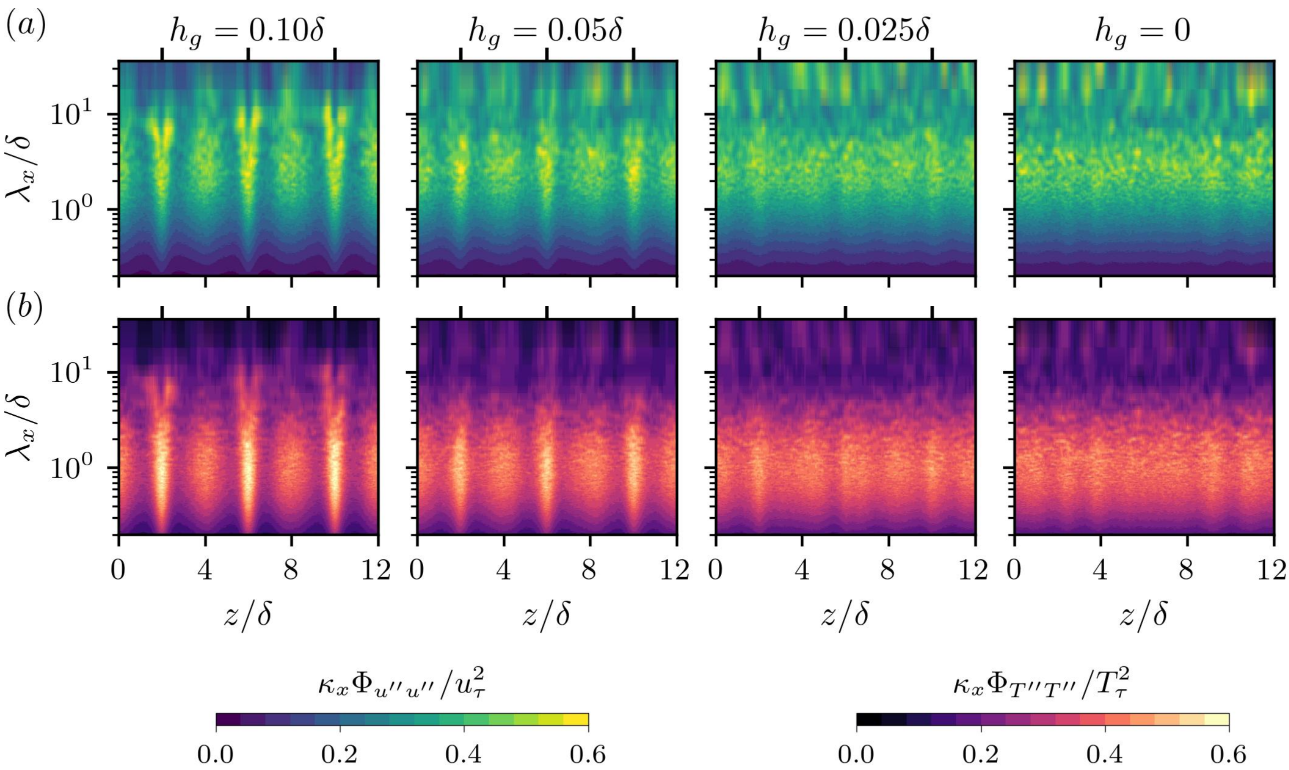

Figure 4. Pre-multiplied streamwise velocity spectra $\kappa_x \Phi_{u''u''}(\lambda_x, z)$ in (a) and temperature spectra $\kappa_x \Phi_{T''T''}(\lambda_x, z)$ in (b) for varying ridge heights h_g at the wall-normal location $y = 0.5\delta$. The black vertical lines at the outer top figure frame indicate the spanwise position of the ridges.

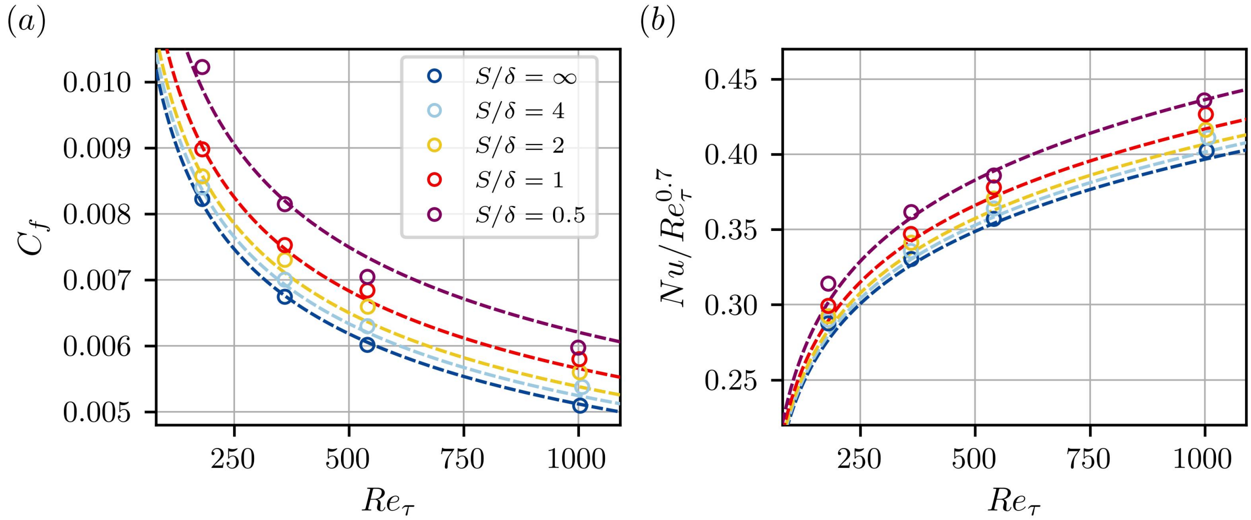

Figure 5. Skin-friction coefficient C_f in (a) and Nusselt number Nu in (b) as a function of Re_τ for different ridge spacings S for cases with $h_g = 0.1\delta$. The dashed lines depict the fitted correlations for C_f and Nu for the shown ridge cases. The correlations are based on a modified version of the smooth wall correlation for C_f by Pope (2000) which are then used in the smooth-wall correlation for Nu proposed by Gnielinski (1976).

source framework for solving turbulence problems on a Cartesian mesh. *SoftwareX* **12**, 100550.

Bauer, C., Sakai, Y. & Uhlmann, M. 2024 Direct Numerical Simulation of Turbulent Open Channel Flow: Streamwise Turbulence Intensity Scaling and Its Relation to Large-Scale Coherent Motions. In *Progress in Turbulence X*, pp. 311–317. Springer Nature Switzerland.

Bou-Zeid, E., Anderson, W., Katul, G. G. & Mahrt, L. 2020 The persistent challenge of surface heterogeneity in boundary-layer meteorology: A review. *Bound.-Layer Meteorol.* **177** (2).

Gautier, R., Laizet, S. & Lamballais, E. 2014 A DNS study of jet control with microjets using an immersed boundary method. *Intl J. Comput. Fluid Dyn.* **28** (6-10), 393–410.

Gnielinski, V. 1976 New equations for heat and mass transfer in turbulent pipe and channel flow. *International Journal of*

Chemical Engineering **16** (2), 359–368.

LeMone, M. A. 1973 The Structure and Dynamics of Horizontal Roll Vortices in the Planetary Boundary Layer. *J. Atmos. Sci.* **30** (6), 1077–1091.

Pope, S. B. 2000 *Turbulent Flows*. Cambridge University Press.

Schäfer, K. 2023 Turbulent large-scale structures over heterogeneous surfaces. PhD thesis, Karlsruhe Institute for Technology (KIT), Kalsruhe, Germany.

Schäfer, K., Frohnapfel, B. & Mellado, J. P. 2022 The effect of spanwise heterogeneous surfaces on mixed convection in turbulent channels. *J. Fluid Mech.* **950**, A22.

Stroh, A., Schäfer, K., Forooghi, P. & Frohnapfel, B. 2020*a* Secondary flow and heat transfer in turbulent flow over streamwise ridges. *Int. J. Heat Fluid Flow* **81**, 108518.

Stroh, A., Schäfer, K., Frohnapfel, B. & Forooghi, P. 2020*b* Rearrangement of secondary flow over spanwise heterogeneous roughness. *J. Fluid Mech.* **885**.

Vanderwel, C. & Ganapathisubramani, B. 2015 Effects of spanwise spacing on large-scale secondary flows in rough-wall turbulent boundary layers. *J. Fluid Mech.* **774**.

Wang, Z.-Q. & Cheng, N.-S. 2006 Time-mean structure of secondary flows in open channel with longitudinal bedforms **29** (11), 1634–1649.

Wangsawijaya, D. D., Baidya, R., Chung, D., Marusic, I. & Hutchins, N. 2020 The effect of spanwise wavelength of surface heterogeneity on turbulent secondary flows. *J. Fluid Mech.* **894**.

Wyngaard, John C. 2010 Turbulence in the Atmosphere.

Zampiron, A., Cameron, S. & Nikora, V. 2020 Secondary currents and very-large-scale motions in open-channel flow over streamwise ridges. *J. Fluid Mech.* **887**, A17.